Original Article

Fabrication of novel nanofiber composed of gelatin/alginate with zirconium oxide NPs regulate orthodontic progression of cartilage degeneration on Wnt/β-catenin signaling axis in MC3T3-E1 cells

Hua Zhao

Department of Stomatology, Second Hospital of Shanxi Medical University, No.382, Wuyi Rd, Xinghualing District, Taiyuan, Shanxi, 030013, China

ARTICLE INFO

ABSTRACT

Natural macromolecules like alginate and gelatin are employed to create medication delivery systems that are both safe and effective. Zirconium nanoparticles (ZrO_2 NPs) have been proposed as a means of enhancing the alginate-gelatin hydrogel's physical and biological properties. This study combines the synthesis of the biopolymers gelatin and alginate nanofibers with nanoparticles of zirconium oxide (GA/NF— ZrO_2 NPs). UV, XRD, FTIR, and SEM were used to characterize the synthesized nanofibers. The expression of osteogenic genes was analyzed by western blotting and qualitative real-time polymerase chain reaction (qRT-PCR). Based on our findings, MC3T3-E1 cells are performed for cell viability, apoptosis and reactive oxygen species production by GA/NF— ZrO_2 NPs through the Wnt/β-catenin signaling pathway. Cell migration was accelerated at 75 μg/mL concentration after 24 h of damage in a scratch wound healing assay. Proliferation of the MC3T3-E1 cell line was also detected. GA/NF—ZrO_2 NPs influenced the osteogenic variation of MC3T3-E1 cells by inducing autophagy. Furthermore, the impact of obstruction on the temporomandibular joint (TMJ) is a subject of ongoing discussion and analysis within the context of animal models. Coordinated GA/NF—ZrO_2 NPs on biomaterial nanofibers could be used to introduce physical signals for modifying MC3T3-E1 responds for orthodontic engineering constructs.

© 2024, The Japanese Society for Regenerative Medicine. Production and hosting by Elsevier B.V. This is an open access article under the CC BY-NC-ND license (http://creativecommons.org/licenses/by-nc-nd/4.0/).

1. Introduction

The field of orthodontics for adults has expanded steadily during the past three decades. The percentage of adults receiving orthodontic treatment increased from 15.4 % in 1981 to 21.0 % in 2017 [1]. The number of adult patients seen by British Orthodontic Society members in private practice increased by 5% in 2018 compared to 2016, according to a study conducted that year. One of the most exciting developments of the 21st century, nanotechnology is at the forefront of the technological revolution by exploiting materials on the nanoscale. Due to their potential to communicate with biological and molecular process, nanomaterials have garnered a lot of attention in biomedical research in recent decades [2]. In most cases, the end result of orthodontic treatment is an intercept that is morphologically stable, aesthetically pleasing, and functionally sound. However, there is a wide range of possible outcomes due to factors such as the degree and kind of malocclusion, treatment technique, patient participation, and the capacity for growth and adaptation of hard and soft tissues [3]. Morphological analysis of the condyle of the mandible of a rat model with apparent cartilage degradation was used to assess the onset sequence of alterations within subchondral bones and cartilage degradation. Bone pro-resorptive factors (M-CSF, RANKL, and OPG) and skeletal pro-formative aspects (Runx2, and VEGF) in the mandible condylar tendon of these rats were also assessed by measuring their mRNA and protein levels [4]. The diagnosis of temporomandibular joint disorder (TMD) is frequently made by dentists and orthodontic specialists [5]. In light of this, numerous investigations into the relationship between TMD and its putative etiologic variables have been done [6]. To achieve this goal and to generate the non-matching cusp-to-fossa relative, 2 or 4 M in different sets of rats were developed to be orthodontically shifted unique positions [7]. Wound dressing, muscle production scaffolds, and drug delivery systems are only few of the many medical uses for natural hydrogels such polycarbohydrates and proteins [8]. Marine brown algae

are the source of alginates (AL, polysaccharides). AL's gelling properties improve after it forms a compound with divalent cations like calcium cation. However, the ionotropy between calcium ions and monovalent cations has an effect on them, leading to the dissolution of alginate [9]. Because of their accessibility, controlled breakdown, and biocompatibility, nanofibers manufactured since food-grade biopolymers are favored in the diet sector [10,11]. For the first time, a comprehensive evaluation of the automatic, physical, electrical, viscoelastic, and cellular biocompatibility of an innovative electroconductive hydrogel constructed on alginate/gelatin with varied absorptions of CNFs has been prepared. Hydrolysis of collagen yields gelatin, a solid biopolymer that lacks flavor and color. Fish, bovine, and porcine gelatin are just examples of the several types that can be distinguished by their origins [12]. This study's fish gelatin contains 85–92 % protein in addition to water and mineral salt. Gelatin is versatile in its processing and has promise biocompatibility and biodegradability [13]. Zirconium oxide (ZrO_2) is a extensive group breach (5.0–5.5 eV), thermally stable, chemically inert, and non-toxic transition metal oxide [14]. ZrO_2 creates a strong covalent bond (Zr–O), which makes the monoclinic structure durable at moderate temperatures, especially room temperature [15]. To elucidate the osteo inductivity of TiO_2 and ZrO_2 NP action, we examined their effects on the survival, oxidative stress, structure, and osteogenic reactions of MC3T3-E1 osteoblasts following co-culture [16]. Zirconia implants have been shown to have improved osseointegration in *In vivo* studies, and ZrO-related materials, such as ZrO_2 layers and ceramics, have been used as bone transplants in the past. Because of its chemical inertness, biocompatibility, and excellent mechanical qualities [17], ZrO_2 is a suitable option for the construction of bone frames [18]. Biphasic implants based on polymeric materials are currently being considered for the therapy of osteochondral defects [19]. Multiple genetic pathways work together to control the osteogenic reaction of cells to physical stimulus. The Wnt/β-catenin signing lane is an example of one of these. Micro-nanofold topology is hypothesized to have a major impact on osteogenic differentiation through autophagy. Wnt/- β-catenin signaling may play a part in its function [20]. Morphological analysis of the mandibular condyle of a previously described rat model by apparent cartilage degradation was performed to assess the beginning process of changes in the subchondral bones and the degradation in cartilage. Bone proresorptive factors M-CSF, RANKL, and OPG, bone pro-formative factors Runx2, and VEGF in the mandibular condylar cartilage of these rats were also assessed by measuring their mRNA and protein levels. Here, we focus on making nanocomposite hydrogels using alginate, gelatin [21], and ZrO_2 NPs for reinforcement, biodegradation, and mechanical features, with the biodegradation and mechanical properties being tuned by varying the amount of ZrO_2 NPs. Runx2 and OSX gene expression research using RT-PCR and western blotting. In addition, the effects of occlusion connection and hydrogel-cultured MC3T3-E1 cells on cell survival, cell proliferation, and apoptosis were investigated *in vitro*.

2. Materials and methods

2.1. Synthesis of alginate gelatin coated zirconium oxide NPs

The 6 wt% OA solution was mixed with the 15 % GEL solution in 5 mL of a 37 °C agitator. The same solution was then cross-linked using a combination of 0.1 g alginate and 0.05 g gelatin to make nanofiber (GA/NF). After 2 min at 37 °C, a flawless gel was formed after the initial gelation was noticed in 4–5 s. Freeze-drying (Alpha 2, 4, Martin Christ, Germany) the hydrogels at 80 °C for 24 h yielded the final powder. After agitating the 6 wt% OA solution for 5 min, 1.5, 1, and 0.25 wt percents of ZrO_2 were added to the vial. After

5 min of stirring, we added 5 mL of 15 wt% GEL to the mixture. GA/NF were added as cross-linker agents and the remaining solutions had been combined for 2 min. We freeze-dried the samples at −80º Celsius for 24 h. About 2-cm-diameter scaffolds with 1-cm-thickness were created [22].

2.2. Characterizations of GA/NF–ZrO$_2$ NPs

X-ray diffractometer (Siemens Co., Germany) employing Cu target radiation at a wave number of 1.5406 A∘ and a scanning rate of 0.05° per 1 s. We used a Fourier Transform Infrared (FTIR) spectrophotometer (IRPrestige-21, Shimadzu Co., Japan) to analyze the mat and determine how its chemical composition has changed. The instrument scanned from 600 to 4000 cm^{-1}. Field emission scanning electron microscopy (FESEM, MIRA3, TeScan Co., Czech Republic) at 15 kV was used to analyze the nanofibers' shape and crystal structure of GA/NF–ZrO$_2$ NPs. By selecting 70 nanofibers at random from each SEM picture, the average diameters of the nanofibers were calculated using the free distribution analysis application ImageJ (NIH, Bethesda, MD, USA). It had been heated at an intensity of 10 C/min from 20 to 600 °C beneath a nitrogen flow velocity of 40 ml/min. This was accomplished with the aid of an inverted fluorescent microscope (model CKX53; Olympus Co., Japan). The resuscitation rates of nanofiber-encapsulated probiotic strains were measured [4].

2.3. Polymerase chain reaction (PCR) with quantifiable results

To get cDNA, we utilized a Prime Script RT reagent Kit (TaKaRa) for converse transcription after isolating total RNA with Trizol reagent (Invitrogen, CA). For our qRT-PCR tests, we utilized TB Green premix Ex *Taq*II (TaKaRa) and cycled the thermocycler at 95º for 30 s, and 95º for 5 s for a total of 40 cycles. Quantitative real-time polymerase chain reaction (qRT-PCR) was completed with primers for runt-related transcription factor 2 (Runx2), Osterix (OSX), glyceraldehyde-3-phosphate dehydrogenase (GAPDH), and beta-catenin. Fold-changes in expression stages were calculated using the 2−ΔΔCT method after the CT value was used to quantify gene expression. This includes the sequences 5′-CTGGCGGTGCAA-CAAGAC-3′, 5′-AACAGCGGAGGCATTTCG-3′, 5′-GAGCAAAGTCA-GATGGGTAAGT-3′, 5′-TCAAGAAGGTGGTGAAGCAGG-3′, and 5′-TCAAAGGTGGAGGAGTGGGT-3' [9].

2.4. The western blotting method

The proteins present in the complete cell were taken out using RIPA lysis solution, specifically the product provided by Invitrogen. The bicinchoninic acid assay was employed to assess the protein content. The protein samples, which were of same concentration, were subjected to separation on sodium dodecyl sulfate-polyacrylamide gels (SDS-PAGE) afterward transported electrochemically onto poly vinyl difluoride films (Millipore, Bedford, MA). The membranes were incubated at 36 °C for a duration of 1 h in a Tris-buffed saline with 0.1 % tween (TBST) solution supplemented with 5 % nonfat milk. Following the rinsing step with TBST, the cell membrane was exposed to an incubation process at a temperature of 4 °C for a duration of 24 h, during which the primary antibodies were mixed and introduced. After being subjected to three washes in TBST, the membrane was subjected to a 2-h incubation at room temperature with subordinate antibodies targeting Runx2, β-catenin, OSX, LC3, p62, and GAPDH. The examination was conducted utilizing an enhanced chemiluminescence (ECL) method provided by Pierce Chemical (Rockford). The density of each blot was assessed by means of the Image J program industrialized through the National Institutes of Health (NIH) [23].

2.5. Differentiation of osteogenic cells

MC3T3-E1 seeds were sown on surfaces with different shapes and textures. A density of 1×10^5 cells/well was used on a 12-well plate, and the cells were cultured until a fusion rate of 70 %–80 % was achieved. After that, we replaced the growing media with a medium specifically designed to promote osteogenic variation. After seven days of bone-forming induction ones, the cultivated cell supernatant was taken out and pressed at 4 °C for 15 min to get rid of any waste or dead cells. Formerly, the specified procedures for measuring ALP activity using a commercially available monitoring kit (Solarbio) were followed. After inducing bone for 21 days, the cells were secure with 4 % paraformaldehyde at 26 °C temperature and humidity for 15–30 min. The cells were bathed in a staining solution made of alizarin red and used to highlight calcium deposits [20].

2.6. Cell culture and maintenance

For this study, we used the mouse pre-osteoblast MC3T3-E1 cell line that we received from Shanghai Cell Bank. We supplemented the DMEM by 10 % FBS, 100 U/mL penicillin, and 100 U/mL streptomycin for our MC3T3-E1 cell culture. The cells were grown in moistened state at 37 °C by 95 % air and 5 % CO_2.

2.7. The cytotoxicity test on MC3T3-E1 cell lines

The MC3T3-E1 cell line was subjected to an MTT experiment to determine the cytotoxicity of LPS. After 24 h of incubation, MC3T3-E1 cells were seeded (5000 cells/well) in triplicate onto 96-well plates and preserved with Zirconium nanofibers (0–75 μg/ml) for 24, 48, and 72 h. In order to determine if zirconium provides protection cells were preserved with LPS for 24 h with or deprived of 4 ng/ml sodium selenite [9]. After 4 h of incubation in the dark with 5 % CO_2 at 37 °C, 10 μl of MTT (5 mg/mL) the substance applied to each well. After cell lysis, 150 μl of DMSO was put into each well. Using a microplate reader (Thermo Fisher Scientific, Inc., Pittsburgh, PA, USA), we determined the absorbance at 490 nm after 5 min. Three separate tests were conducted to ensure reliability. By comparing the sample's OD to the OD of the control sample, the proportion of viable cells may be calculated.

$$\text{Percentage of cell viability} = \frac{\text{OD value of experimental samples}}{\text{OD value of experimental controls}} \times 100$$

2.8. Cell proliferation assay

The Cell Counting Kit-8 (CCK-8) test (Dojindo Molecular Technologies; Kumamoto, Japan) was used to determine the survival rate of the cells. Five thousand cells were placed in each well of a 96-well plate. After adding ZrO_2 NPs to the 96-well plates at serial concentrations of 0, 10, 20, 40, 60, 80, 100, and 150 μg/mL and incubating at 37 °C with 5 % CO_2 for 1, 3, and 7 days, with or without N-acetyl-L-cysteine (NAC) to prevent ROS formation, the results were compared. The untreated group served as the control. Then, the CCK-8 test was carried out by adding 110 μL detecting reagent to every well, and the 96-well plates were allowed to incubate for an additional 2 h at 37 °C. After 2 h of reaction time, the reagents for testing were transferred to a fresh 96-well plate, while the precipitated NPs and cell were left in the initial plate to avoid interfering with the analytical assay. The microplate reader

(SpectraMax M5, Molecular Devices, Sunnyvale, CA, USA) assessed the optical density (OD) of each well at a fixed wavelength of 450 nm. There were six of each treatment done.

2.9. Scratch assay on MC3T3-E1 cell lines

To get a confluent layer, MC3T3-E1 cells were grown in 12-well plates for 24 h at 1.5×10^5 cells per well. With a 100 μl sterile pipette tip, we scratched over the cell layer. After removing the media, the cells were washed in PBS to get rid of any remaining particles. After that, 300 μL of DMEM was added, and the dish was irradiated. The plates were then reintroduced into the incubator after being refilled with DMEM to a final volume of 1 mL per well. At 0 and 24 h after irradiation, images were taken using phase contrast microscope and fluorescent microscope. All experiments were done three times to ensure accuracy was used for the image capture. The scratch's size was calculated using Image J. By observing how much of the scratch was still bare 24 h after irradiation, we were able to determine how quickly the wound was healing.

2.10. ROS exposure of GA/NF–ZrO₂ NPs

Based on the methodology, with some modifications [15], 2,7-dichlorofluorescin diacetate (DCFH-DA) was used to enumerate intracellular reactive oxygen species (ROS) production in response to exposure to GA/NF–ZrO_2 NPs. Two distinct methods, fluorometric analysis and fluorescence microscopy imaging, were cast-off to appraise the emergence of reactive oxygen species (ROS). Ten thousand cells were covered hooked on separately well of a 96-well culture plate with a black bottom for use in fluorometric analysis. The cells were permissible to stick to the plates for one day in a CO_2 incubator at 37º Celsius. The cells were then exposed for 24 h to different doses of GA/NF–ZrO_2 NPs. After the allotted time for exposure has passed, the cells were splashed twofold with HBSS. The cells were then incubated for 30 min at 37º Celsius in 1 mL of a DCFH-DA solution. After the cells were lysed in an alkaline solution, the cellular components were mixed with the lysate and centrifuged at 2300 g for 15 min to separate the cellular debris from the nanoparticles. The fluorescence intensity was restrained using a micro plate reader (Synergy-HT, BioTek, USA) at an innervation wavelength of 485 nm and 520 nm on a size of 200 μl of the precipitate relocated to a 96-well plate. Percentages of fluorescence intensity relative to control cells were used to quantify the values. To examine intracellular fluorescence, this study made use of a clear 96-well plate holding a consistent number of cells (1×10^4 cells/well). The analysis was performed with an OLYMPUS CKX 41 fluorescent microscope. At a magnification of 20×, images of the cells were taken.

2.11. Apoptosis with GA/NF–ZrO₂ NPs

After transduction, MC3T3-E1 cells were treated to GA/NF–ZrO_2 NPs. These cells' reactivity to apoptosis was evaluated using 7-actinomycin D (7AAD) and Annexin V phycoerythrin (PE). The cellular samples were analyzed after they were pickled with cisplatin at an attention of 25 mol/l for 48 h. Cells that were only preserved with salt water served as the control group.

2.11.1. Methods involving animal experiments

All experiments on animals must first be approved by the Animal Experimentation Committee. Forty male SD rats (SPF grade) were cared for and weighed at five weeks of age, averaging 156 ± 18 g. Breeding conditions consist of temperatures between 20º and 22º Celsius and humidity between 40 and 60%. Each day has

an equal amount of daylight and nighttime. Randomization was used to divide rats (n = 10 per group) into four treatment groups: control, 2 weeks, 4 weeks, and 8 weeks. Throughout the variation dated, the rats were free to eat and drink as they pleased, but they were required to abstain from food and water during the light portion of the experiment so that the equipment wouldn't be accidently removed. The device consists of a crown incision in the upper jaw, a slanted directing dish, and an extraoral retention aid. According to functional orthopedics theory, the mandibles of rats moved higher down a slope with each mouth closure [23].

2.11.2. Create tooth planetary and establish the fossa's non-matching cusp occlusal connection

The cusp and fossa do not have a matching occlusal relation, as predicted by the method given above [23]. The primary maxilla tooth on the leftward and the initial inframaxillary molar on the accurate were shifted using orthodontic flexible rubber-bands in the EXP-I group. After 7 days, we switched out the rubber bands for a self-curing material to keep the spaces open. At 2, 4, and 8 weeks after band placement, all six rats (3 males and 3 females) were euthanized. The 2nd group had the same occlusion procedures as the 1st group during the first 4 weeks of the study. At the commencement of the 5th week, we used rubber bands to further disrupt occlusion by placing single among the left 2nd and 3rd maxilla teeth and the other between the right 2nd and 3rd mandibular molars. At 2, 4, and 8 workweeks afterward the second rubber bands were implanted, all six rats (3 males and 3 females) were euthanized. Rubber bands or self-curing glue were used throughout the treatment, however considerable caution was used to avoid contact with the opposing teeth. We were able to successfully deploy two rubber bands or blobs of self-curing resin to different sites within 5 min. Once a week, the rats were checked for the self-curing mastic, and once a day to make sure the bands made of rubber were still on. Whenever any did not exist upon inspection, the operation was repeated immediately. The rest of the process was the same as described in detail.

2.11.3. Preparation of tissues

The gadget was used to kill the rats at the beginning of the study, after 2 weeks, after 4 weeks, and after 8 weeks. Suffocating the rodents using carbon dioxide gas. The left femoral condyle was removed from the rest of the femur and the surrounding tissue was cut away as soon as possible after death. After 30 days in 10 % EDTA for decalcification, drying, and embedding in PBS, the material is complete. Condyles were serially sectioned (5 m) the mid-sagittal level for morphological and immunohistochemical examination. Micro-CT imaging was done after the accurate condyle was fixed in 4 % paraformaldehyde. Three rats had all six condylar of their TMJs removed and ice-covered at $-80\ ^{\circ}$C for RNA abstraction. Condyle subchondral bone, located 3 mm below the cartilage-bone contact, was transacted for RNA [24].

2.11.4. Staining and grading for histology

Hematoxylin and eosin (HE) streak was castoff to analyze the condyles for histological changes [7]. Three major parts of the distal condyle joint have the same amount of cartilage as anterior and posterior halves. All hypertrophic layers in the central two-thirds of the condylar cartilage received the treatment. Each treatment area was 300 m squared. At the halfway, the cartilage thickness was measured. Thomas et al. [25] graded condylar cartilage using the OARSI and Mankin methods.

2.11.4.1. Statistical analysis. The experiments were conducted in triplicates. The data were analyzed using GraphPad Prism and are presented as the mean $\pm$ standard error median. The comparison

between different groups was conducted using one-way analysis of variance (ANOVA) with post hoc Tukey's multiple analysis test. Furthermore, all analysis was subjected to statistical analysis utilizing two-way ANOVA and Bonferroni post-test.

3. Result and discussion

3.1. Characterization

The FTIR spectra of Ge, DAA, and the DAA/Ge hydrogel demonstrated a schematic crosslinking between the two substances. Typical protein peaks can be seen as absorption peaks at 1639 and 1540 cm^1 in the Ge spectra; these peaks are associated with the stretching vibration of the NAH in amide I and II, respectively. The creation of C@N bonds is responsible for the emergence of bands at 1626 and 1560 cm^1 that are caused by the formation of Schiff's bases. Prepared DAA/Ge/Ag nanocomposite UV−Vis absorbance spectra [2]. Fig: 1 A displays the UV−Vis absorbance spectra at 260 nm for GA/NF−ZrO$_2$ NPs. The FT-IR spectrum to show how sodium alginate and gelatin compounds interact with one another. FTIR analysis was used to confirm chemical crosslinking between GEL and OA, yielding results consistent with those previously reported. Alginate, oxidized alginate, and hydrogels with ZrO$_2$ NPs, as seen in FTIR spectroscopy. After oxidation, the aldehyde group's symmetric vibration was identified as a new band at 1730 cm^1 [22]. Alginate, oxidized alginate, and ZcO NP-containing scaffolds are shown off in their FTIR spectra. Vibrational frequencies of related functional groups were used to interpret the identifying bands in the IR spectra of sodium alginate and gelatin (Fig. 1: B). The glycan peaks in alginate's spectrum are also easily identifiable. For O−C−O and O−C bending phases in guluronic and mannuronic units, respectively, the bands at 1116 and 1032 cm^1 are specified [31]. In the spectral analysis of gelatin, the peak for amide A was located at 3320 cm^{-1}, the peaks for amide II at 1533 and 1445 cm^{-1}, and the peak for amide III at 1235 cm^{-1}. The FTIR spectra of NGs, which has a peak at 1680 cm^1, reveals that gelatin and carrageenan gum have formed covalent connections [29]. The X-ray diffraction (XRD) method is mostly used to determine the type of phase a material is and the typical size of its crystals. Fig. 1: C XRD ornamentation of GA/NF−ZrO$_2$ NPs. similarly synthesized The X-ray diffraction (XRD) patterns of the BmimCF3COO IL-synthesized ZrO$_2$ NPs. The results showed reflection planes ($2\theta = 30.270$) that match towards the planes (101), related of the tetragonal sparkling scheme made up of ZrO$_2$ NPs (JCPDS 01-080-2155) [3].

3.2. qRT-PCR and western blotting

Osteogenic related marker genes, such as RUNX2 and OSX, have their mRNA and protein amounts evaluated using qRT-PCR and western blotting techniques, as shown in Fig. 2. Quantitative real-time polymerase chain response examination of osteogenic gene expression in MC3T3-E1 after 7 and 14 days of treatment on gelatin, alginate, GA/NF, and GA/NF−ZrO$_2$ NPs (I). II) The Expression of Runx2, p62 and Osx proteins in MC3T3-E1 cells cultured for 7 and 14 days on gelatin, alginate, GA/NF and GA/NF−ZrO$_2$ NPs was investigated by Western blotting. Finally, on days 7 and 14, fold changes were seen for Runx2, p62 Osx, GAPDH, and β-catenin. Three independent tests preconditioned the data. The expression of β-catenin and its relative abundance in the nucleus (a) and the cytoplasm (b) Western blotting analysis of GAPDH and β-catenin expression (Fig. 3). Similar increases in RUNX2 and VEGF mRNA and protein levels were also observed in the condylar tissue of 12-week EXP groups, indicating an uptick in endochondral ossification activity. However, Runx2 and vascular endothelial growth factor have been linked to fostering osteoclast genesis. PGC-1a in the context of
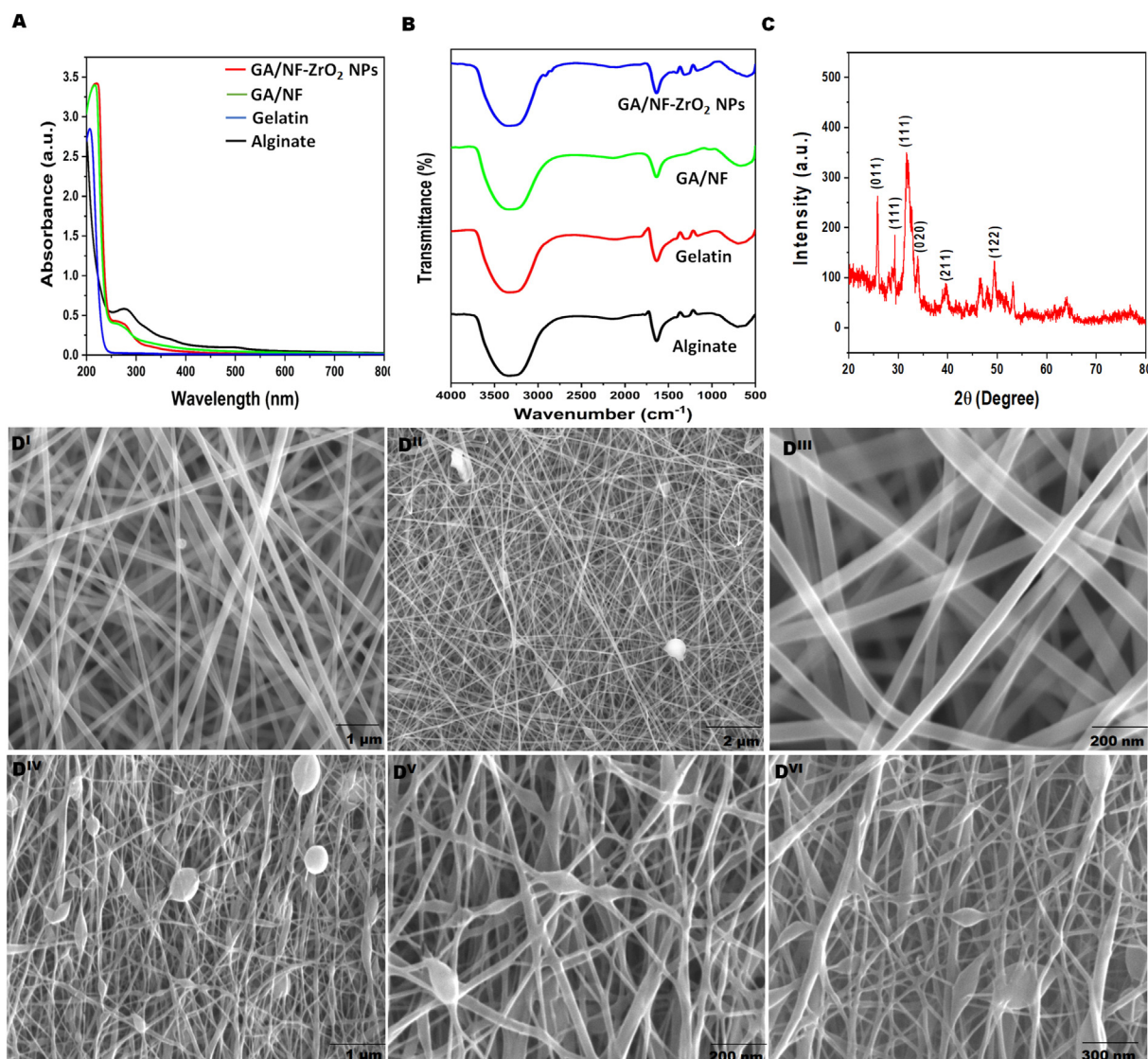
Fig. 1. UV-Spectroscopy A); FTIR analysis B); XRD spectrum C); SEM images of D^I Alginate, D^{II} Gelatin, D^{III} Gelatin/alginate, D^{IV} GA/NF, D^V & D^{VI} GA/NF–ZrO$_2$ NPs at different magnification.

TFEB suppression has not reduced aggregation, which may imply a decrease in bone formation [7]. The mRNA level of OPG appears to decrease first in the current research. Our data shows that PGC-1a is upfront of TFEB in the regulation of transcription of the autophagy-lysosome axis [6], where it promotes turnover of proteins and aggregation repression through coactivating the expression of TFEB. The transcript levels of COL2 and SOST was found to be reduced by IHC and PCR in the overload group, whereas that of MMP3 and β-catenin was shown to be elevated. Wnt/β-catenin signaling pathway becomes active in the course of mandible condylar cartilage deterioration and subchondral loss of bone caused by excessive functional orthopedic force (OFOF) [8].

3.3. Osteogenic differentiation

The activity of alkaline phosphatase (ALP) was employed as an indicator of osteogenic differentiation. After 3 days, 7 days, 14 days, and 21 days of cell culture on the substrates, the ALP activity was measured. Activation of alanine aminotransferase (ALP) and osteogenic differentiation (B) at various incubation times (Fig. 4). There

was a topographically-dependent variation in ALP expression. Topographic significance of MC3T3-E1 is demonstrated. W27 suppressed ALP expression in comparison to the Flat control, while W0.5, W3, and W10 all increased it. W3 had the greatest effect on ALP expression. Osteogenic development in mesenchymal stem cells (MSC) was shown to be inhibited by activation of the conventional WNT channel by WNT-1 or WNT-3a in *In vitro* investigations [20].

### 3.4. Effect on MC3T3-E1 cells and viability

Phase, fluorescent, of MC3T3-E1 cells allowed to examine the implications of cell shape. Surface shape has a major impact on how cells align themselves. The orientation of growing cells occurs at random. Cell viability tests were conducted on MC3T3-E1 cell lines, as shown in Fig. 5. Data from A) phase contrast microscopy, B) fluorescent microscopy, C) cell viability under varying incubation conditions, D) cell orientation as a percentage. 50 μg/ml gelatin, alginate, GA/NF, and GA/NF–ZrO$_2$ NPs were used to expose the cells. The same sort of thing was seen in cells cultivated on larger
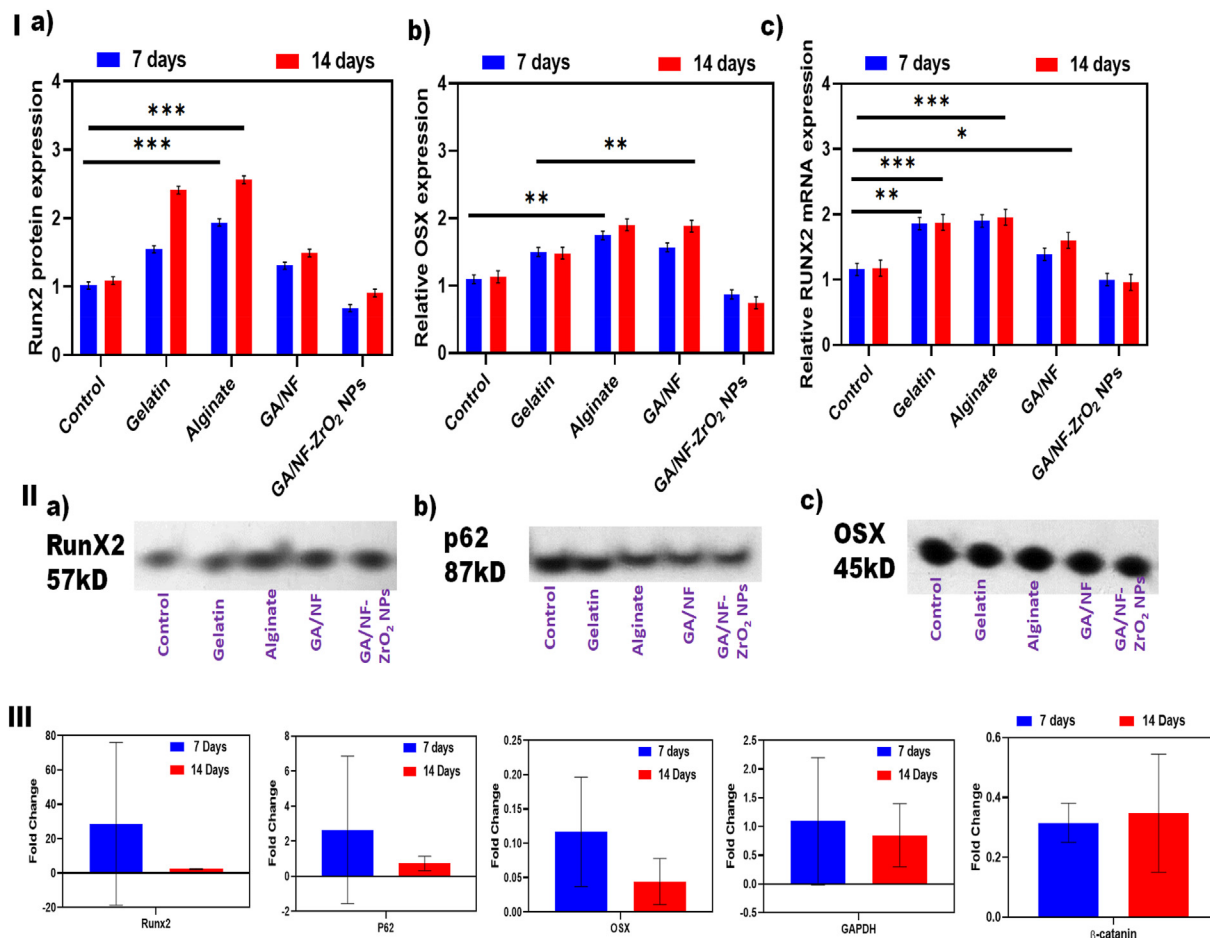
Fig. 2. I) Expression of the osteogenic genes Runx2 (a), Osx (b) and Runx2mRNA relative gene expression (c) in MC3T3-E1 after 7 and 14 days of incubation on gelatin, alginate, GA/NF and GA/NF—ZrO₂ NPs by quantitative real-time polymerase chain reaction. II) Expression of Runx2, p62 and Osx proteins in MC3T3-E1 cells grown for 7 and 14 days on gelatin, alginate, GA/NF and GA/NF—ZrO₂ NPs was analyzed using Western blotting. III) Fold changes were noted for 7 and 14 days for Runx2, p62 Osx, GAPDH and β-catenin. Data was on condition that by three self-determining assays and shown as mean ± SD (*p<0.05).

topographies. The CCK-8 assess was used towards quantify MC3T3-E1 cell viability after 1d and 3d of incubation on the various topographies. Cell growth is clearly supported on all substrates for at least 3 days. More specifically, For 1d and 3d growth, there were more cells on the W3 surface than on both other surfaces. how selenium influences apoptosis in osteoblasts. *In vitro*, we discovered that LPS dramatically condensed the capability of MC3T3-E1 cells, induced apoptosis, and upped ROS generation [23]. The
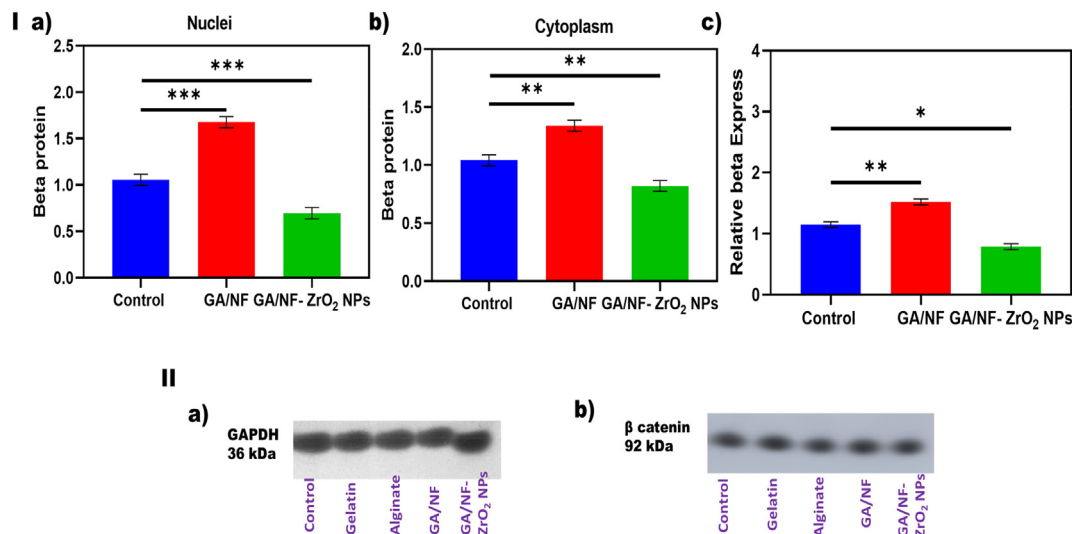
Fig. 3. I) β-protein expression on nuclei (a) cytoplasm (b) and relative β catenin expression II) Expression of GAPDH and β catenin through western blotting.
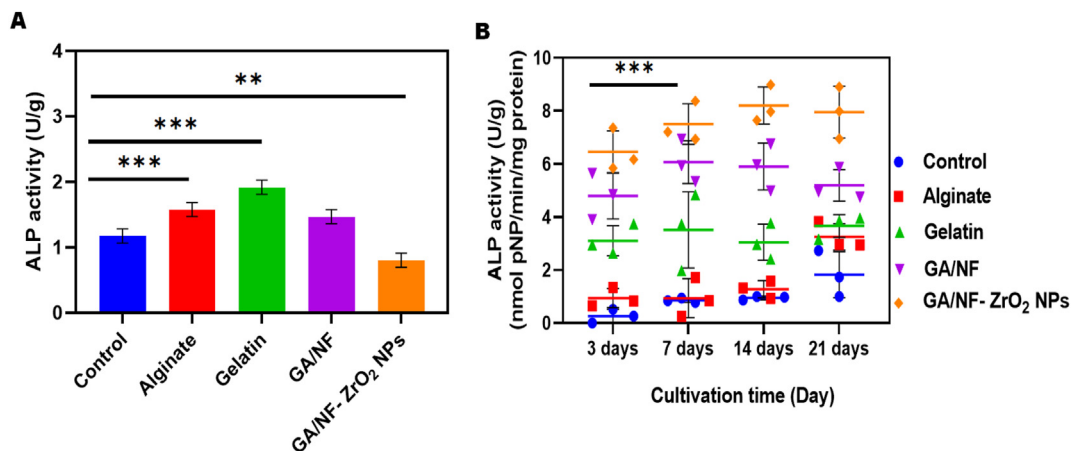
Fig. 4. Osteogenic differentiation A) ALP activity B) ALP activity with different incubation time.

surface morphology of a cell has a significant impact on the cell's orientation. A cell's orientation during growth on Flat is completely random, but on W0.5 it is marginally orientated in the general direction of the roughness. Larger topographies highlighted the directional structure of cells in culture. The CCK-8 assay was used to quantify MC3T3-E1 cell feasibility subsequently 1day and 3day of incubation on the various topographies. Cell growth is clearly supported on all substrates for at least 3 days. especially, the cell density on the W3 layer for 1day and 3day culture outpaced that on both of the surfaces. disk has the ability to enhance the explosion, distinction, and variation of MC3T3-E1 cells [20], as well as

encourage macrophages to undergo a transition to the anti-inflammatory M2 lineage. The MTT results show that both scaffolds with and without ZnO nanoparticles are safe to use. When cells were exposed to the scaffolds, cell viability decreased with time [31]. The viability values in this investigation were higher than 83.9 %, and the visualizations show no statistically significant variations across the samples. Reliable with the outcomes of a preceding study [29], materials containing nanoparticles (NGs) showed improved cell viability. The initial step in the regulation of cell proliferation, migration, and differentiation by materials is cell adhesion. Cell proliferation on various substrates after 1, 3, and 7
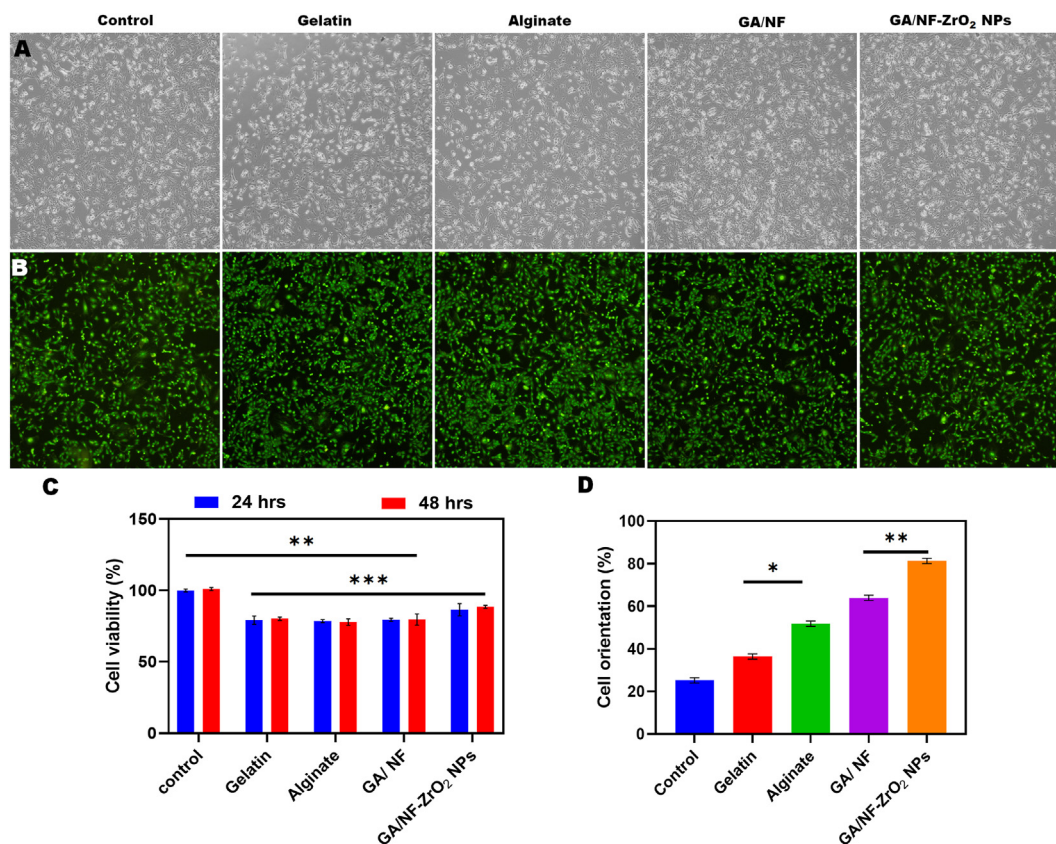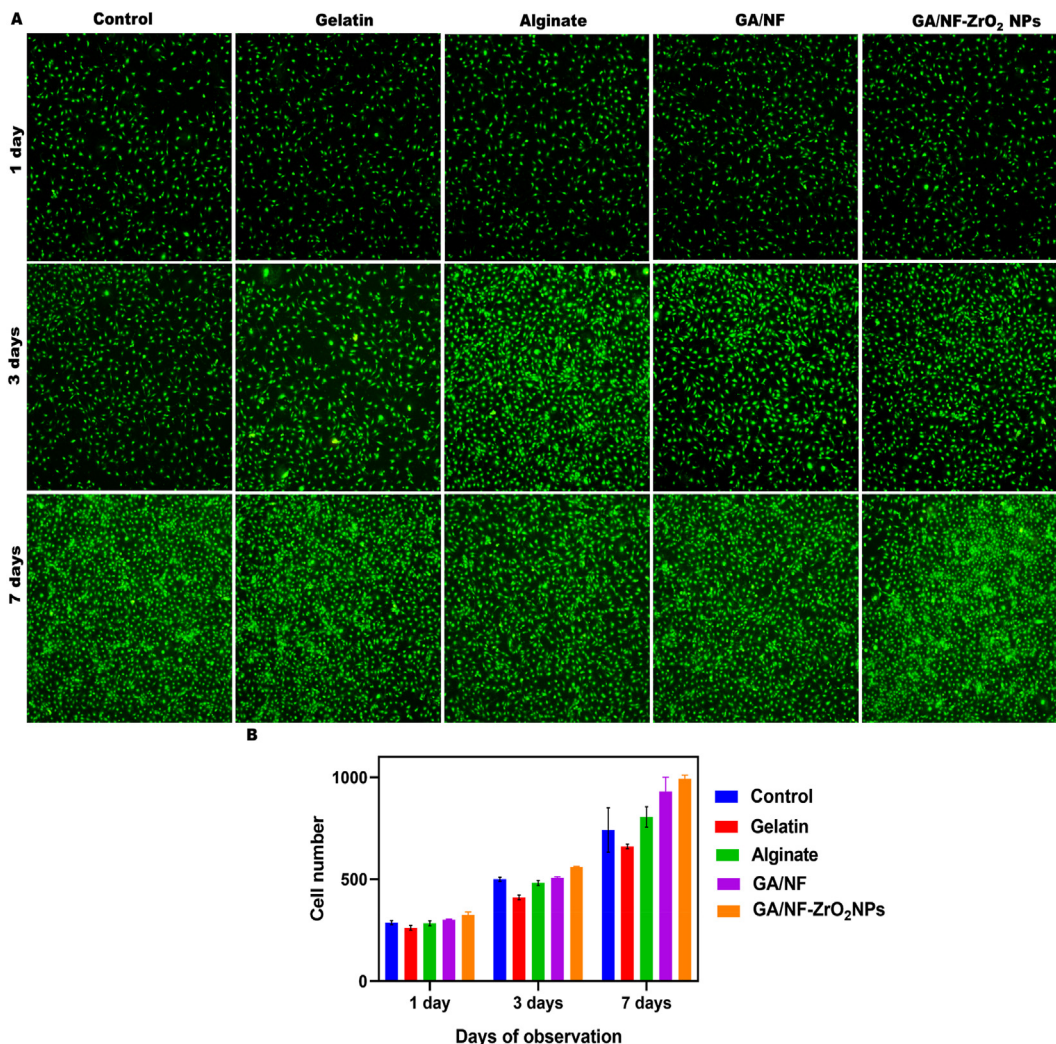

Fig. 5. Cell viability was performed for MC3T3-E1 cell lines A) Phase contrast microscopic images at 100 μm, 10× magnification B) Fluorescent images 100 μm, 10× magnification C) Cell viabilty with different incuabtion D) Percentage of cell orientation.

Fig. 6. Cell proliferation assay on MC3T3-E1 cell lines on gelatin, alginate, GA/NF and GA/NF−ZrO$_2$ NPs (A) Fluorescence images of cells cultured in three different matrix at 1,3 and 7 days and the Scale bars 100 μm. (b) The number of MC3T3-E1 cells adhered to the surface of materials at three different days of observation and are statistically significant P < 0.01.
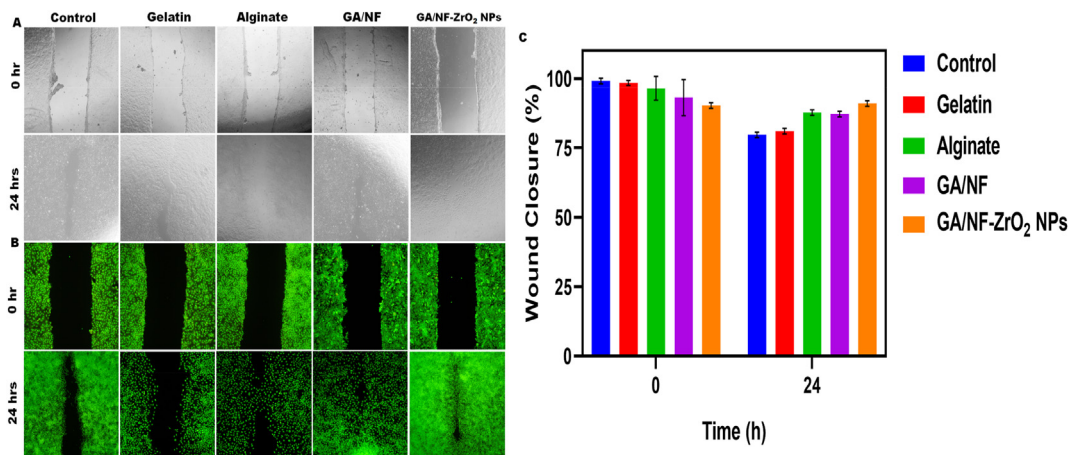

Fig. 7. The scratch assay to investigate the wound healing of MC3T3-E1 cell lines indicate the area of the scratch at 0, 12, and 24 h after the treatment. A) Phase contrast B) Fluorescent Pictures shows the groups treated with gelatin, alginate, GA/NF, GA/NF−ZrO$_2$ NPs with the better healing rate than control group 100 μm, 10× magnification. C) Scratch wound area was measured 0,12 and 24 h post treatment. P < 0.001 statistically significance.
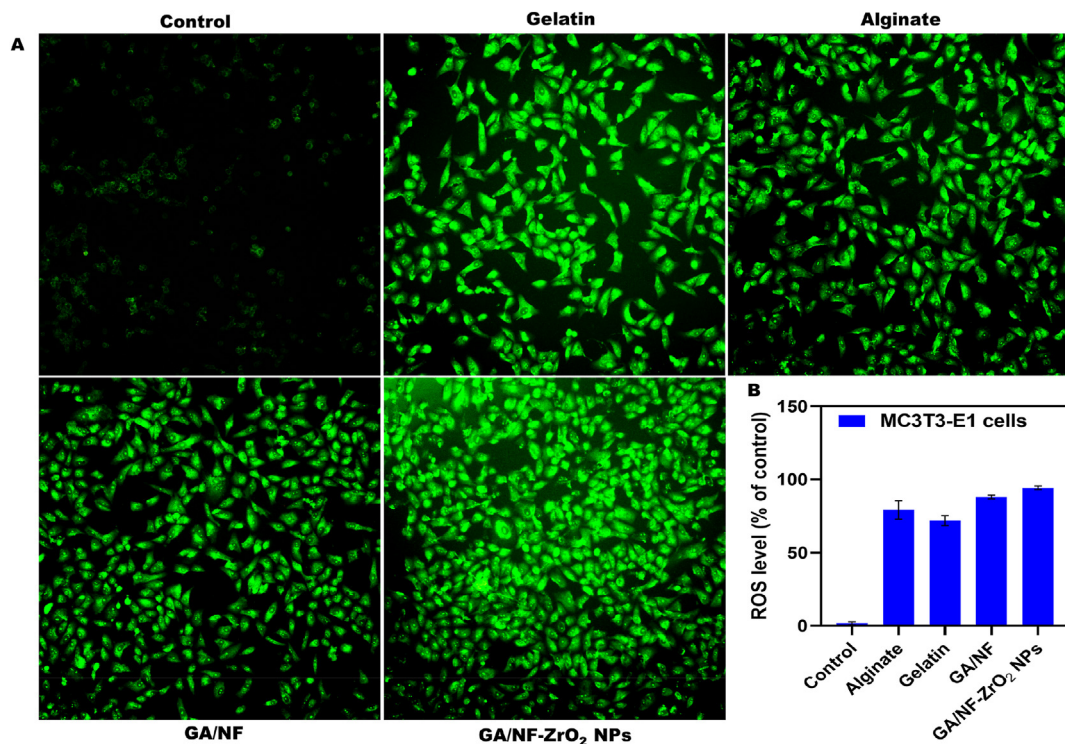
Fig. 8. MC3T3-E1 cell lines was used to oxidative stress exposed with gelatin, alginate, GA/NF and GA/NF−ZrO$_2$ NPs OLYMPUS CKX 41 fluorescent microscope images were used 100 μm, 10× magnification (A); Percentage of ROS level on MC3T3-E1 cell lines (B).
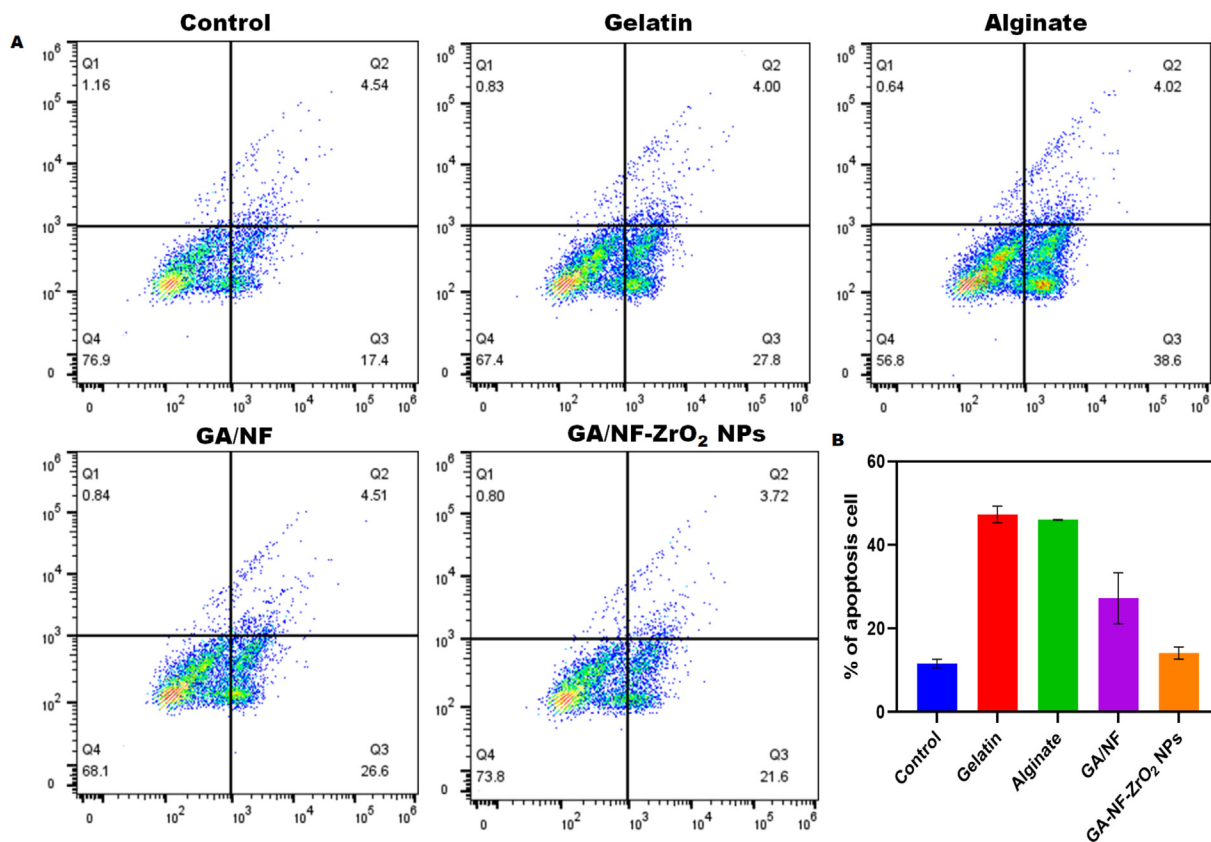
Fig. 9. Flow cytometry was used to regulate the apoptosis percentage. Treatment of MC3T3-E1 cells with gelatin, alginate, GA/NF and GA/NF−ZrO$_2$ NPs are not malignant are preserved rather than undergoing cell death (A). The apoptosis percentage were analyzed for MC3T3-E1 cell lines with statistical evaluation (B).
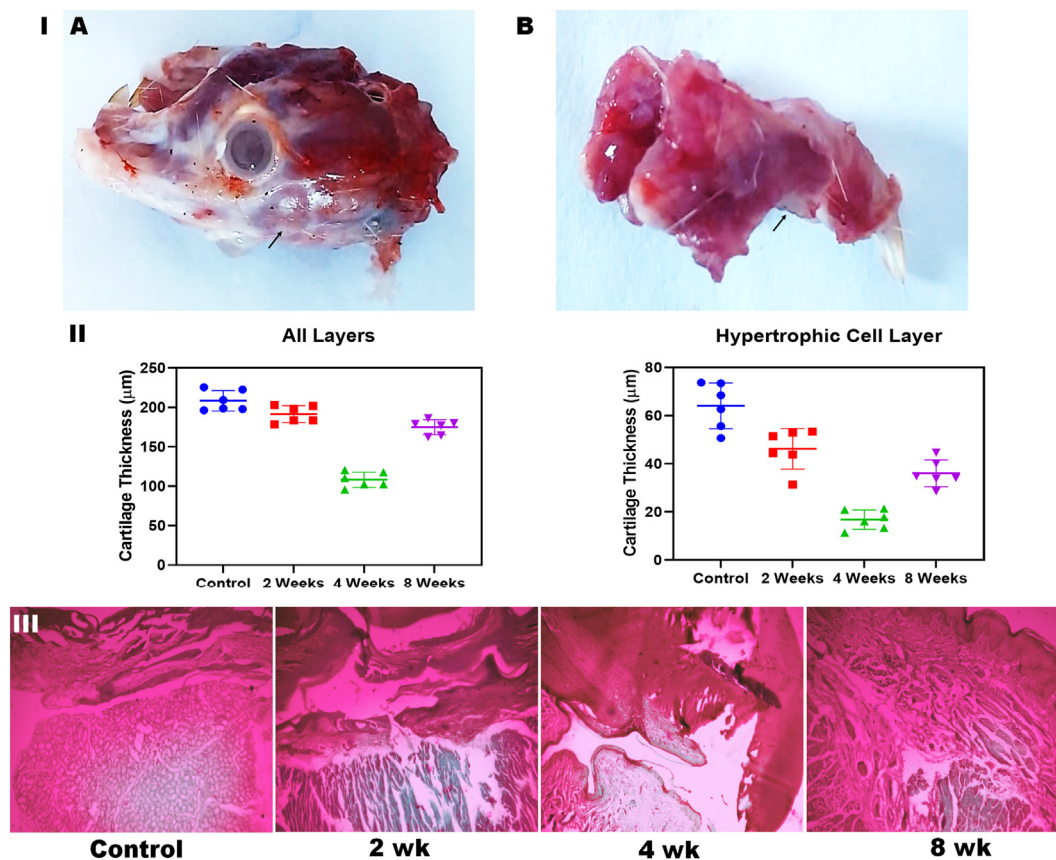
Fig. 10. Intraoral views of the mandible advanced appliance model. I (A&B) Endochondral and subchondral bone layer; II) Total cartilage thickness and thickened layer thickness among all groups. The layers of condylar cartilage, especially the thickened layer, were thinner in the loading group than in the control group. (*P < 0.001). (III) Condyle head histological layer (Fibrous layer) depicted in schematic form. The condylar cartilage layers, especially the hypertrophic layer, were thinner in the overload group compared to the control group.

days. MC3T3-E1 cell proliferation experiment on gelatin, alginate, GA/NF, and GA/NF–ZrO$_2$ NPs (Fig. 6: A). Scale bars, 100 μm, are superimposed on fluorescence pictures of cells cultivated in each of the three matrices at 1, 3, and 7 days (Fig. 6: B). Significantly higher numbers of MC3T3-E1 cells attached to surfaces during the course of three days of observation (P < 0.01). The number of cells linked to each substance also increased steadily over time, as seen in the diagram. During the same time, the cell number cultivated on the CCM group was significantly greater compared to that on the MCM group and PCM group. FA is a plant-based chemical with a clear effect on cell growth. After 24 and 48 h of treatment with ZrO$_2$ NPs, the results demonstrated that NAC had a negative effect on cell survival produced by the nanoparticles. After NAC inhibition, the survival of cells was upheld for 24 h regardless of the concentrations of ZrO$_2$ NP administration until the very uppermost level (150 μg/mL) [24].

3.5. Scratch wound healing assay

The scratch assay was carried out, and photographs were taken at 0 and 24 h post-treatment. A scratch experiment was performed on MC3T3-E1 cell lines to examine wound healing. The area of the scratch was measured at 0 and 24 h post-treatment (Fig. 7: A). Fig. 7B shows a phase contrast. Fluorescent Pictures show a faster rate of healing in the groups given gelatin, alginate, GA/NF, and GA/NF–ZrO$_2$ NPs compared to the control group (Fig. 7: C) After 24 h of treatment, the size of the scratches was evaluated. The significance level is at P < 0.001. The irradiated groups were contrasted to a

control group that had not been exposed to radiation. Red light's impact on how quickly wounds heal. 24 h after treatment, the graph shows a statistically significant increase in wound healing with dosages of 5 mW/cm^2 for 13 min (3.9 J/cm^2), 10 mW/cm^2 for 5 min (3 J/cm^2), 8 min (4.8 J/cm^2), and 15 mW/cm^2 for 5 min (4.5 J/cm^2). In addition, the group exposed to 10 mW/cm^2 for 8 min (4.8 J/cm^2) had a significantly higher wound healing rate 24 h later compared to the other groups. Wound closure in the irradiated groups was nearly identical to that in the control group 48 h after the treatment ended [26]. A reliable scratch apparatus for conducting in vitro scratch assays with high levels of consistency and repeatability. When compared to a method based on pipette tips, the tests showed that it performed better in creating scratches in 96-well plates that were consistent in width and position [27]. Half an hour after treatment, the control group had fully healed scratch wounds in vitro, while the groups treated with BiodentineTM and ProRoot® MTA had not. The cells were cultured in a medium containing 25 % extraction from the various materials. Cells grown in regular media served as the control. As A red dot line, which represents the initial border of the edge of the scratched wound, is visible in the representative images of the scratch areas [28]. Specifically, to prevent senescence-inducing over-damage to neighbouring cells, meticulous consideration should go into scratch generation. To avoid damaging too much of the culture plate surface in the migration zone and extracellular matrix, it is best to use a plastic pipette tip instead of a hypodermic needle or scalpel when scratching [29]. Similar findings demonstrated the importance of rheodynamic control of the microenvironment of cells in fostering

a physicochemical milieu conducive to enhanced cell motility and wound healing.

3.6. ROS in MC3T3-E1 cells

An upshot of oxidative stress, ZrO$_2$ NPs caused alterations in cell morphology and an increase in membrane micro viscosity. After ZrO$_2$ NP treatment, the concentration-dependent ROS (free oxygen radicals) level in 3T3-E1 cells was measured. MC3T3-E1 cell lines was used to oxidative stress exposed with gelatin, alginate, GA/NF and GA/NF–ZrO$_2$ NPs OLYMPUS CKX 41 fluorescent microscope images were used A); Percentage of ROS level on MC3T3-E1 cell lines (Fig. 8). Similar results detected the We measured reactive oxygen species (ROS) levels in 3T3-E1 cells upon treatment with TiO$_2$ and ZrO$_2$ NPs and discovered that both NPs generated considerable ROS formation in concentration-dependent manners, with ZrO$_2$ NPs inducing more intense oxidative stress effects. The ROS scavenger NAC could also reduce the abnormally high ROS levels. These findings supported a crucial part played by reactive oxygen species (ROS) in TiO$_2$- and ZrO$_2$-induced cell cytotoxicity [16].

3.7. Apoptosis on MC3T3-E1 cell lines

Apoptosis is a system of cell demise that removes aging and defective cells to preserve cell biology. Treatment with oxide metal nanoparticles, such as TiO$_2$, ZnO, Si, and Ag, has been linked to apoptosis in certain research [19]. The level of apoptosis was controlled with flow cytometry. Cell viability is maintained rather than lost after treating cancerous MC3T3-E1 cells with gelatin, alginate, GA/NF, or GA/NF–ZrO$_2$ nanoparticles (NPs) (A). Statistical analysis (B) was used to determine the apoptosis percentage of MC3T3-E1 cell lines (Fig. 9). Similarly, apoptotic/necrotic cell formation in 3T3-E1 cells was induced by TiO$_2$ and ZrO$_2$ NPs in time/concentration-dependent manners, which coincided with the observed reduction in cell viability. This phenomenon demonstrated that ZrO$_2$ NPs caused faster and more powerful apoptotic effects. Other research [17] confirmed that ZrO$_2$ NPs triggered substantial apoptotic and inflammatory processes in MSTO cells.

3.8. Condylar cartilage degradation and associated histology were brought on functional orthopaedic force

Overloaded mechanical orthopaedic force was delivered to rats for varying time periods in order to observe the degradation of condylar cartilage [30]. Advanced appliance model of the mandible, shown from within the mouth. First, the total thickness of the endochondral and subchondral bones layers in all groups; second, the total thickness of the cartilage and the thickened layer. Loading participants had thinner condylar cartilage layers, particularly the thickened layer. Condyle head histological layer (Fibrous layer) depicted in schematic form. The condylar cartilage layers, especially the hypertrophic layer, were thinner in the overload group compared to the control group (Fig. 10). Similar findings demonstrated that a rise in condylar volume, with the rise in volume attributable to a rise in condylar cartilage thickness. Adaptive changes in condylar volume can cause new bone to grow and cause a shift in condylar shape [8]. The second scenario should result in increased occlusal disharmony, which could further injure the compromised joint [31]. Previous research suggested that mandible advancement (MA) appliances might deliver effective orthopaedic forces to the inframaxillary condyle, and modify cartilage development then bone construction. However, the primary diseased alteration in TMJ-OA is the degradation of condylar cartilage due to overload stress [26]. As a result, TMJ OA contributes to the

overloading of articular cartilage and the subchondral bone. In the progression of maxillary condylar cartilage degradation and subchondral bone damage caused by excessive practical orthopaedic stress, the Wnt/β-catenin axis is stimulated [8].

4. Conclusion

Gelatin and alginate nanofibers coated with zirconium NPs were successfully produced under room temperature and at ambient condition (GA/NF–ZrO$_2$ NPs). Crystalline particle, functional groups, morphological features, and particle size were all discussed in the characterization study. Using RT-PCR and western blotting, Countenance of the osteogenic genes Runx 2, Osx and Runx2 mRNA relative gene expression found that GA/NF–ZrO$_2$ NPs influenced the osteogenic variation of MC3T3-E1 cells through the Wnt/β-catenin axis. According to the results of this study, the size of the synthesized NPs has a role in determining whether or not MC3T3-E1 cells differentiate into osteoblasts. MC3T3-E1 cells were used in cytotoxicity tests, wound scratch assay and proliferation. Degenerative changes to the mandible condylar cartilage are exacerbated when orthodontic tooth movement occurs in more quadrants, leading to increased TMJ injury. According to an *In vivo* investigation. These data are indicative of the function of occlusion in TMD. These results provide novel approaches for tissue modification and regenerative therapies involving the temporomandibular joint.

Ethical statement

The study was approved by the Ethical Committee of the Second Hospital of Shanxi Medical University (NO. 2023-YX-063).

Declaration of competing interest

There are no conflicts for the present investigation.

References

[1] Chow L, Goonewardene MS, Cook R, Firth MJ. Adult orthodontic retreatment: a survey of patient profiles and original treatment failings. Am J Orthod Dentofacial Orthop 2020;158(3):371–82. https://doi.org/10.1016/j.ajodo.2019.09.010.
[2] Abou-zeid RE, Awwad NS, Nabil S, Salama A, Youssef MA. International Journal of Biological Macromolecules Oxidized alginate/gelatin decorated silver nanoparticles as new nanocomposite for dye adsorption. Int J Biol Macromol 2019;141:1280–6. https://doi.org/10.1016/j.ijbiomac.2019.09.076.
[3] Tapak NS, Nawawi MA, Tjih ET, Mohd Y, Ab Rashid AH, Abdullah J, et al. The synthesis of zirconium oxide (ZrO2) nanoparticles (NPs) in 1-butyl-3-methylimidazolium trifluoroacetate (BMIMCF3COO) for an amperometry phenol biosensor. July Mater Today Commun 2022;33:104142. https://doi.org/10.1016/j.mtcomm.2022.104142.
[4] Ma Y, Qi P, Ju J, Wang Q, Hao L, Wang R, et al. Gelatin/alginate composite nanofiber membranes for effective and even adsorption of cationic dyes. no. December 2018 Compos B Eng 2019;162:671–7. https://doi.org/10.1016/j.compositesb.2019.01.048.
[5] Mohlin B, Axelsson S, Paulin G, Pietilä T, Bondemark L, Brattström V, et al. TMD in relation to malocclusion and orthodontic treatment: a systematic review. Angle Orthod 2007;77(3):542–8. https://doi.org/10.2319/0003-3219(2007)077. 0542:TIRTMA]2.0.CO;2.
[6] Tsunemi T, Ashe TD, Morrison BE, Soriano KR, Au J, Roque RA, et al. PGC-1a rescues Huntington's disease proteotoxicity by preventing oxidative stress and promoting TFEB function. Sci Transl Med 2012;4(142). https://doi.org/10.1126/scitranslmed.3003799.
[7] Jiao K, Niu LN, Wang MQ, Dai J, Yu SB, Liu XD, et al. Subchondral bone loss following orthodontically induced cartilage degradation in the mandibular condyles of rats. Bone 2011;48(2):362–71. https://doi.org/10.1016/j.bone.2010.09.010.
[8] He Z, Liu M, Zhang Q, Tian Y, Wang L, Yan X, et al. Wnt/β-catenin signaling pathway is activated in the progress of mandibular condylar cartilage degeneration and subchondral bone loss induced by overloaded functional orthopedic force (OFOF). Heliyon 2022;8(10):e10847. https://doi.org/10.1016/j.heliyon.2022.e10847.

[9] Ye M, Shi B. Zirconia nanoparticles-induced toxic effects in osteoblast-like 3T3-E1 cells. Nanoscale Res Lett 2018;13. https://doi.org/10.1186/s11671-018-2747-3.

[10] Serafin A, Murphy C, Rubio MC, Collins MN. Printable alginate/gelatin hydrogel reinforced with carbon nanofibers as electrically conductive scaffolds for tissue engineering. February Mater Sci Eng C 2021;122:111927. https://doi.org/10.1016/j.msec.2021.111927.

[11] Luo W, Song Z, Wang Z, Wang Z, Li Z, Wang C, et al. Printability optimization of gelatin-alginate bioinks by cellulose nanofiber modification for potential meniscus bioprintingvol. 2020; 2020.

[12] Tonsomboon K, Strange DGT, Oyen ML. Gelatin nanofiber-reinforced alginate gel scaffolds for corneal tissue engineering. Proceedings of the annual international conference of the IEEE engineering in medicine and biology society. EMBS; 2013. p. 6671–4. https://doi.org/10.1109/EMBC.2013.6611086.

[13] Tanne K. Degenerative changes of articular cartilage in association with mechanical stimuli. Japanese Dental Science Review 2008;44(1):38–47. https://doi.org/10.1016/j.jdsr.2007.10.004.

[14] Hossain N, Mobarak MH, Hossain A, Khan F, Mim JJ, Chowdhury MA. Advances of plant and biomass extracted zirconium nanoparticles in dental implant application. Heliyon 2023;9(5):e15973. https://doi.org/10.1016/j.heliyon.2023.e15973.

[15] Radu RD, Drăgănescu D. Present and future of ZrO2 nanostructure as reservoir for drug loading and release. Coatings 2023;13(7):1–21. https://doi.org/10.3390/coatings13071273.

[16] Kapur A, Felder M, Fass L, Kaur J, Czarnecki A, Rathi K, et al. Modulation of oxidative stress and subsequent induction of apoptosis and endoplasmic reticulum stress allows citral to decrease cancer cell proliferation. No. January: Nature Publishing Group; 2016. p. 1–14. https://doi.org/10.1038/srep27530.

[17] Ma D, Yang W. Engineered nanoparticles induce cell apoptosis. potential for cancer therapy 2016;7(26).

[18] Yuan Y, Wu Y, Suganthy N, Shanmugam S, Brindhadevi K, Sabour A, et al. Biosynthesis of zirconium nanoparticles (ZrO2 NPs) by Phyllanthus niruri extract: characterization and its photocatalytic dye degradation activity. Food Chem Toxicol 2022;168(April):113340. https://doi.org/10.1016/j.fct.2022.113340.

[19] Brunner TJ, Wick P, Bruinink A. In vitro cytotoxicity of oxide nanoparticles : comparison to asbestos , silica , and the effect of particle solubility 2006;40(14):4374–81.

[20] Zhang Q, Zhang Q, Yan X, Wang L, Yuan X. Wrinkled topography regulates osteogenesis via autophagy-mediated Wnt/β-catenin signaling pathway in MC3T3-E1 cells. March Arch Oral Biol 2023;151:105700. https://doi.org/10.1016/j.archoralbio.2023.105700.

[21] Begines B, Arevalo C, Romero C, Hadzhieva Z, Boccaccini AR, Torres Y. Fabrication and characterization of bioactive gelatin-alginate-bioactive glass composite coatings on porous titanium substrates. ACS Appl Mater Interfaces 2022;14(13):15008–20. https://doi.org/10.1021/acsami.2c01241.

[22] Ghanbari M, Salavati-Niasari M, Mohandes F, Firouzi Z, Mousavi SD. The impact of zirconium oxide nanoparticles content on alginate dialdehyde-gelatin scaffolds in cartilage tissue engineering. J Mol Liq 2021;335:116531. https://doi.org/10.1016/j.molliq.2021.116531.

[23] Wang M, Sun L, Yu SB, Liu X, Jiao K, Wang GW, et al. Degenerative changes in rat condylar cartilage induced by non-matching occlusion created by scattered orthodontic teeth-moving. Cranio 2012;30(4):286–92. https://doi.org/10.1179/crn.2012.043.

[24] Franco WF, Galdino MV, Capeletti LR, Sberowsky BH, Vieira RA, Figueiredo AC, et al. Photobiomodulation and mandibular advancement modulates cartilage thickness and matrix deposition in the mandibular condyle. Photobiomodulation, Photomed Laser Surg 2020;38(1):3–10. https://doi.org/10.1089/photob.2019.4640.

[25] Thomas M, Fronk Z, Gross A, Willmore D, Arango A, Higham C, et al. Losartan attenuates progression of osteoarthritis in the synovial temporomandibular and knee joints of a chondrodysplasia mouse model through inhibition of TGF-b1 signaling pathway. Osteoarthritis Cartilage 2019;27(4):676–86. https://doi.org/10.1016/j.joca.2018.12.016.

[26] Giannakopoulos E, Katopodi A, Rallis M, Politopoulos K. The effects of low power laser light at 661 nm on wound healing in a scratch assay fibroblast model. Laser Med Sci 2023:1–10. https://doi.org/10.1007/s10103-022-03670-5.

[27] Chen S, bin Abdul Rahim AA, Mok P, Liu D. An effective device to enable consistent scratches for in vitro scratch assays. BMC Biotechnol 2023 Aug 28;23(1):32.

[28] Manaspon C, Jongwannasiri C, Chumprasert S, Sa-Ard-Iam N, Mahanonda R, Pavasant P, Porntaveetus T, Osathanon T. Human dental pulp stem cell responses to different dental pulp capping materials. BMC Oral Health 2021 Dec;21(1):1–3.

[29] Cormier N, Yeo A, Fiorentino E, Paxson J. Optimization of the wound scratch assay to detect changes in murine mesenchymal stromal cell migration after damage by soluble cigarette smoke extract. JoVE 2015 Dec 3;(106):e53414.

[30] Rashed MZ, Sharawy MM. Histopathological and immunocytochemical studies of the effect of raised occlusal vertical dimension on the condylar cartilage of the rabbit. Cranio : J Cranio-Mandibular Pract 1993;11(4). https://doi.org/10.1080/08869634.1993.11677981.

[31] Fang L, Ye Y, Tan X, Huang L, He Y. Overloading stress—induced progressive degeneration and self-repair in condylar cartilage. Ann N Y Acad Sci 2021;1503(1):72–87. https://doi.org/10.1111/nyas.14606.